

Memristor-Based Hyperchaotic Maps and Application in Auxiliary Classifier Generative Adversarial Nets

Han Bao¹, Member, IEEE, Zhongyun Hua¹, Member, IEEE,
Houzhen Li¹, Graduate Student Member, IEEE, Mo Chen¹, Member, IEEE,
and Bocheng Bao¹, Member, IEEE

Abstract—With the nonlinearity and plasticity, memristors are widely used as nonlinear devices for chaotic oscillations or as biological synapses for neuromorphic computations. But discrete memristors (DMs) and their coupling maps have not received much attention, yet. Using a DM model, this article presents a general three-dimensional discrete memristor-based (3-D-DM) map model. By coupling the DM with four 2-D discrete maps, four examples of 3-D-DM maps with no or infinitely many fixed points are generated. We simulate the coupling coefficient-depended and memristor initial-boosted bifurcation behaviors of these 3-D-DM maps using numerical measures. The results demonstrate that the memristor can enhance the chaos complexity of existing discrete maps and its coupling maps can display hyperchaos. Furthermore, a hardware platform is developed to implement the 3-D-DM maps and the acquired hyperchaotic sequences have high randomness. Particularly, these hyperchaotic sequences can be applied to the auxiliary classifier generative adversarial nets for greatly improving the discriminator accuracy.

Index Terms—Auxiliary classifier generative adversarial nets (AC-GANs), chaos complexity, discrete map, discrete memristor (DM), hardware implementation, hyperchaotic sequence.

I. INTRODUCTION

MEMRISTOR, owning the features of nonlinearity and plasticity, is a nonlinear electronic device that links flux and charge organically [1]. It can memorize its memristance or memductance by regulating the internal attribute of charge or flux [2]. The memristor has greatly raised the development of nonlinear oscillating circuits for its specific nonlinearity [3].

Manuscript received August 19, 2021; revised October 2, 2021; accepted October 6, 2021. Date of publication October 12, 2021; date of current version May 6, 2022. This work was supported by the National Natural Science Foundation of China under Grant 62071142 and Grant 51777016. Paper no. TII-21-3629. (Corresponding author: Bocheng Bao.)

Han Bao, Houzhen Li, Mo Chen, and Bocheng Bao are with the School of Microelectronics and Control Engineering, Changzhou University, Changzhou 213164, China (e-mail: charlesbao0319@gmail.com; leehzh@126.com; mchen@cczu.edu.cn; mervinbao@126.com).

Zhongyun Hua is with the Harbin Institute of Technology, Shenzhen, Shenzhen 518055, China (e-mail: huazyum@gmail.com).

Color versions of one or more figures in this article are available at <https://doi.org/10.1109/TII.2021.3119387>.

Digital Object Identifier 10.1109/TII.2021.3119387

It also has various applications in neuromorphic computations because of its synaptic plasticity [4].

Chaotic behaviors can be exhibited using continuous or discrete dynamical systems under specific parameter and initial settings [3]. A chaotic system has many properties such as the initial sensitivity, topological mixing, and unpredictability [5], [6]. Thanks to these unique properties, chaotic systems have been extensively studied and applied in academic and industrial fields [7]–[9]. Generally, when being regarded as a nonlinear electronic device, the memristor can be introduced into some existing dynamical systems to induce chaotic oscillations with complex dynamics. Due to the introduction of memristors, initial-related multistability was easily emerged in various memristor-based chaotic systems [10], [11].

Generally speaking, the initial-related multistability can be achieved by either drawing the memristors into dynamical systems [3], or leading some periodic functions in offset-boostable systems [12]. These two approaches can make the dynamical systems to generate initial-related equilibrium points, which result in the emergence of multistability. Furthermore, a combination of these two approaches was presented by importing a periodic memductance-based memristor into an offset-boostable system and the generated system can show memristor initial-boosted coexisting plane bifurcations [13]. However, all these efforts were only applied to continuous dynamical systems. Compared with the continuous dynamical systems, discrete dynamical systems have many advantages such as high implementation efficiency. Therefore, to achieve the initial-related multistability in discrete dynamical systems is very appealing. Recently, we have successfully presented a discrete memristor (DM) by discretizing an existing continuous memristor [14]. And then we have constructed a general two-dimensional DM (2-D-DM) map model by coupling the DM with an existing 1-D discrete map, and provided four examples of 2-D-DM maps [15]. The results showed that the 2-D-DM maps can generate hyperchaos with memristor initial-boosted behaviors and the DM can increase the chaos complexity of the existing 1-D discrete map. Similarly, two different kinds of DMs were also developed in [16] and [17], and the DM-based Hénon map and DM-based sine map were designed to exhibit the memristor-induced dynamical effects. With this preliminary idea, this article presents a general three-dimensional DM-based (3-D-DM) map model by coupling the DM with some existing 2-D discrete maps. Four examples of 3-D-DM maps with no or infinitely many fixed points are raised

to acquire hyperchaotic sequences using numerical simulations and hardware experiments. The results show that the DM allows the generated hyperchaotic sequences to be switched by its initials and it can significantly enhance the chaos complexity of 2-D discrete maps. Different from [15] that presented a 2-D-DM map model, this article presents a 3-D-DM map model, which has essential difference with the 2-D-DM map model. In particular, since the examples of 3-D-DM maps have no fixed points or infinitely many fixed points, they are either in specific hidden states or in conventional self-excited states. However, the examples of 2-D-DM maps have only infinitely many fixed points, and thus they are just in conventional self-excited states. Therefore, the 3-D-DM maps show more complex dynamics than the 2-D-DM maps.

In addition, to show the effects of the 3-D-DM maps in applications, this article applies these maps to novel network architecture called generative adversarial nets (GANs) [18]. The GANs have two nets and simulates the zero-sum game in game theory. By alternately training, the generation net in the GANs can generate highly realistic data. With significant properties, the GANs are becoming a more and more important technique in the artificial buildings of natural images and some related functionalities. Recently, GANs and their variants have been successfully applied to numerous applications, such as the super-resolution reservoir simulation [19], wind turbine fault detection [20], intelligent fault diagnosis [21], and imbalanced acoustic event detection [22]. To achieve the training-stability, an extended GANs framework, called the auxiliary classifier GANs (AC-GANs), was proposed for image synthesis [23]. Because vast pseudorandom numbers (PRNs) are required, chaotic sequences generated by lasers were utilized for the latent variables of GANs and the similarity of the generated images in proximity was enhanced [24]. To promote the discriminator accuracy of the AC-GANs, in this article, we first employ the experimentally acquired hyperchaotic sequences of the 3-D-DM maps to generate PRNs, and then use these PRNs as the latent variables of the AC-GANs.

The contributions of this article are summarized as follows.

- 1) A general 3-D-DM map model is presented and four examples of hyperchaotic maps with no or infinitely many fixed points are provided.
- 2) The bifurcation behaviors of the 3-D-DM maps are simulated. The memristor initial-switched hyperchaotic attractors and sequences show the ability of the memristor in enhancing the chaos complexity.
- 3) A hardware platform is developed to implement the 3-D-DM maps to physically acquire the hyperchaotic sequences with high randomness.
- 4) These sequences can be readily employed to generate PRNs and these PRNs can greatly improve the discriminator accuracy of the AC-GANs when they are used as the latent variables.

The rest of this article is organized as follows. Section II presents a general 3-D-DM map model. Section III studies the coupling coefficient-depended bifurcation dynamics and Section IV discusses the memristor initial-boosted bifurcation behaviors. The hardware platform is developed and the chaos-based application in AC-GANs is raised in Section V. Finally, Section VI concludes this article.

II. DISCRETE MEMRISTOR-COUPLED MAP MODEL

By coupling a DM with a 2-D discrete map, this section presents a general 3-D-DM map model.

A. Discrete Memristor Model

Using the forward Euler difference method described in [14], a continuous memristor can be discretized to be a discrete one. Thus, a DM model is described as [15]

$$\begin{aligned} v_n &= M(q_n)i_n = \cos(q_n)i_n \\ q_{n+1} &= q_n + i_n \end{aligned} \quad (1)$$

where the current i_n , voltage v_n , and charge q_n represent the discrete values at the n -th iteration and the charge q_{n+1} denotes the discrete value at the $(n+1)$ -th iteration.

When a discrete sinusoidal current is applied to the input port of DM given in (1), the frequency-relied and initial-relied pinched hysteresis loops are well displayed, which have been detected in [15] detailedly.

B. Memristor-Coupled Map Model

The Hénon map [25], Duffing map [26], and Lozi map [27] are three typical examples of 2-D discrete maps. According to their algebraic equations, a general map model of these 2-D discrete maps can be introduced and described by

$$\begin{cases} x_{n+1} = F(x_n, y_n) \\ y_{n+1} = G(x_n) \end{cases} \quad (2)$$

Equation (2) becomes the Hénon map, Duffing map, and Lozi map when setting $F = 1 - ax_n^2 + y_n$ and $G = bx_n$, $F = ax_n - x_n^3 - by_n$ and $G = x_n$, and $F = 1 - a|x_n| + y_n$ and $G = bx_n$, respectively. Note that the Duffing map here is a little different from its original definition. To unify the representation form of these three existing 2-D chaotic maps, we have exchanged the positions of variables x_n and y_n in the original definition of the Duffing map.

By coupling the DM described by (1) to the 2-D discrete map model given in (2), a general 3-D-DM map model can be constructed and it is described by

$$\begin{cases} x_{n+1} = F(x_n, y_n) \\ y_{n+1} = G(x_n) + k \cos(q_n)y_n \\ q_{n+1} = y_n + q_n \end{cases} \quad (3)$$

where k represents the coupling coefficient. Thus, using the model (3), some specific 3-D-DM maps can be derived by coupling the DM to some existing 2-D discrete maps. This scheme is simple but quite effective. It can improve the chaos complexity of existing 2-D discrete maps.

The fixed point $S = (\bar{x}, \bar{y}, \bar{q})$ of the 3-D-DM map can be solved by the following algebraic equations:

$$\bar{x} = F(\bar{x}, \bar{y}), \bar{y} = G(\bar{x}) + k \cos(\bar{q})\bar{y}, \bar{q} = \bar{y} + \bar{q}. \quad (4)$$

From the third equation of (4), one has $\bar{y} = 0$. As the second equation of (4) satisfies that $G(0) = 0$, i.e., $\bar{x} = 0$, two situations appear in the first equation of (4).

When $F(0, 0) \neq 0$, the 3-D-DM map has no fixed points since (4) has no real solutions. In this situation, the 3-D-DM map is in specific hidden states.

When $F(0, 0) = 0$, the 3-D-DM map has infinitely many fixed points and its fixed points are expressed by

$$S = (\bar{x}, \bar{y}, \bar{q}) = (0, 0, c) \quad (5)$$

where c is a constant depending on the memristor initial.

The stability of the fixed points is characterized by the eigenvalues of Jacobian matrix. The Jacobian matrix of the 3-D-DM map at $S = (\bar{x}, \bar{y}, \bar{q})$ is expressed by

$$\mathbf{J}_P = \begin{bmatrix} J_{11} & J_{12} & 0 \\ J_{21} & k \cos(c) & 0 \\ 0 & 1 & 1 \end{bmatrix} \quad (6)$$

where $J_{11} = \partial F(x_n, y_n)/\partial x_n|_{x_n=0, y_n=0}$, $J_{21} = \partial G(x_n)/\partial x_n|_{x_n=0}$, and $J_{12} = \partial F(x_n, y_n)/\partial y_n|_{x_n=0, y_n=0}$. These three Jacobian elements J_{11} , J_{21} , and J_{12} are determined by the models and parameters of existing 2-D discrete maps.

The characteristic polynomial is obtained from (6) as

$$P(\lambda) = (\lambda - 1)(\lambda^2 - d_1\lambda + d_2) \quad (7)$$

where $d_1 = J_{11} + k \cos c$ and $d_2 = k J_{11} \cos(c) - J_{12} J_{21}$. The two parameters d_1 and d_2 also depend on the initial state of the DM. Thus, the eigenvalues are deduced as

$$\lambda_1 = 1, \lambda_{2,3} = 0.5 \left(d_1 \pm \sqrt{d_1^2 - 4d_2} \right). \quad (8)$$

If $|\lambda_m| < 1$ ($m = 1, 2, 3$), the fixed point is stable; otherwise, it is unstable. As can be found from (8), λ_1 is on the unit circle, whereas λ_2 and λ_3 can be inside or outside the unit circle and their states are depended on d_1 and d_2 . Hence, the fixed points for the 3-D-DM map could be unstable or critical stable.

As a result, when $F(0, 0) = 0$, the fixed points of the 3-D-DM map could be unstable or critical stable. A stable initial point on the phase space will approach to a stable sink. By contrast, an unstable initial point on the phase space will either tend toward a strange attractor, or diverge to infinity. This means that the 3-D-DM map can exhibit the self-excited states.

C. Discrete Memristor-Based Hyperchaotic Maps

By coupling the DM with the Hénon map, Duffing map, and Lozi map, respectively, three specific 3-D-DM maps are yielded from (3) and they are named as 3-D memristor-based Hénon (3-D-MH) map, 3-D memristor-based Duffing (3-D-MD) map, and 3-D memristor-based Lozi (3-D-ML) map, respectively. Table I shows the equations of these 3-D-DM maps and the existing 2-D discrete maps. Moreover, when coupling the DM to a 2-D simple map, a simple 3-D memristor-based (3-D-MS) map can be also built from (3), as shown in the last column of Table I. Therefore, four examples of 3-D-DM map model are presented by coupling the DM to four 2-D discrete maps. Because all the four 3-D-DM maps can show hyperchaotic behaviors, they are also called 3-D-DM hyperchaotic maps.

Because $F(0, 0) \neq 0$, the 3-D-MH map and 3-D-ML map have no fixed points, which results in the specific hidden states.

In contrast, since $F(0, 0) = 0$, the 3-D-MD map and 3-D-MS map have infinitely many fixed points given in (5). For the 3-D-MD map, its Jacobian elements in (6) are calculated as $J_{11} = a$, $J_{12} = -b$, and $J_{21} = 1$, and its eigenvalue parameters in (8) equal to $d_1 = a + k \cos c$ and $d_2 = ka \cos c + b$. Similarly, for

TABLE I
FOUR TYPES OF 3-D DISCRETE MEMRISTIVE HYPERCHAOTIC MAPS

Original Map Models	Memristive Map Models	Map Names
$\begin{cases} x_{n+1} = 1 - ax_n^2 + y_n, \\ y_{n+1} = bx_n. \end{cases}$ (2D Hénon Map)	$\begin{cases} x_{n+1} = 1 - ax_n^2 + y_n, \\ y_{n+1} = bx_n + ky_n \cos q_n, \\ q_{n+1} = y_n + q_n. \end{cases}$	3D-MH Map
$\begin{cases} x_{n+1} = ax_n - x_n^3 - by_n, \\ y_{n+1} = x_n. \end{cases}$ (2D Duffing Map)	$\begin{cases} x_{n+1} = ax_n - x_n^3 - by_n, \\ y_{n+1} = x_n + ky_n \cos q_n, \\ q_{n+1} = y_n + q_n. \end{cases}$	3D-MD Map
$\begin{cases} x_{n+1} = 1 - a x_n + y_n, \\ y_{n+1} = bx_n. \end{cases}$ (2D Lozi Map)	$\begin{cases} x_{n+1} = 1 - a x_n + y_n, \\ y_{n+1} = bx_n + ky_n \cos q_n, \\ q_{n+1} = y_n + q_n. \end{cases}$	3D-ML Map
$\begin{cases} x_{n+1} = ay_n, \\ y_{n+1} = bx_n. \end{cases}$ (2D Simple Map)	$\begin{cases} x_{n+1} = ay_n, \\ y_{n+1} = bx_n + ky_n \cos q_n, \\ q_{n+1} = y_n + q_n. \end{cases}$	3D-MS Map

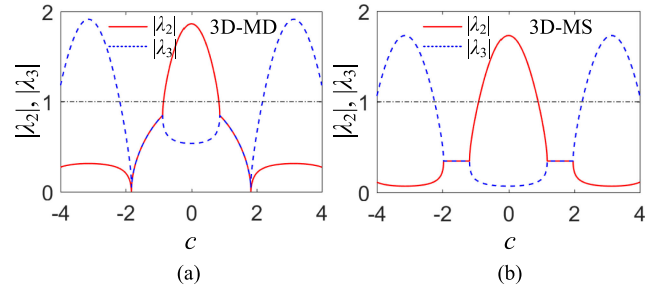


Fig. 1. Values of $|\lambda_2|$ and $|\lambda_3|$ with the variation of the memristor initial c in a full periodic cycle. (a) 3-D-MD map. (b) 3-D-MS map.

the 3-D-MS map, its Jacobian elements in (6) are calculated as $J_{11} = 0$, $J_{12} = a$, and $J_{21} = b$, and its eigenvalue parameters in (8) are expressed as $d_1 = k \cos c$ and $d_2 = ab$. When these related parameters are given, the three eigenvalues in (8) can be calculated and the stabilities of the 3-D-MD and 3-D-MS maps can be easily determined.

First, the typical parameters of the 3-D-MD map are set to $a = 0.4$, $b = 0.2$, and $k = 2$. The values of $|\lambda_2|$ and $|\lambda_3|$ relied on the memristor initial c are plotted in Fig. 1(a) and the unstable intervals of c in $[-\pi, \pi]$ are solved by (8) as

$$\begin{aligned} c \in (-0.8411, 0.8411), & \text{ for } |\lambda_2| > 1; \\ c \in (-\pi, -2.1790) \cup (2.1790, \pi), & \text{ for } |\lambda_3| > 1. \end{aligned} \quad (9)$$

Second, the typical parameters of the 3-D-MS map are determined as $a = 1.2$, $b = 0.1$, and $k = 1.8$. The values of $|\lambda_2|$ and $|\lambda_3|$ associated with c are plotted in Fig. 1(b) and the unstable intervals of c in $[-\pi, \pi]$ are solved by (8) as

$$\begin{aligned} c \in (-0.8992, 0.8992), & \text{ for } |\lambda_2| > 1 \\ c \in (-\pi, -2.2424) \cup (2.2424, \pi), & \text{ for } |\lambda_3| > 1. \end{aligned} \quad (10)$$

Consequently, when c locates in the initial intervals given by (9) or (10), the 3-D-MD or 3-D-MS map is unstable; otherwise, the two maps are critical stable due to $\lambda_1 = 1$.

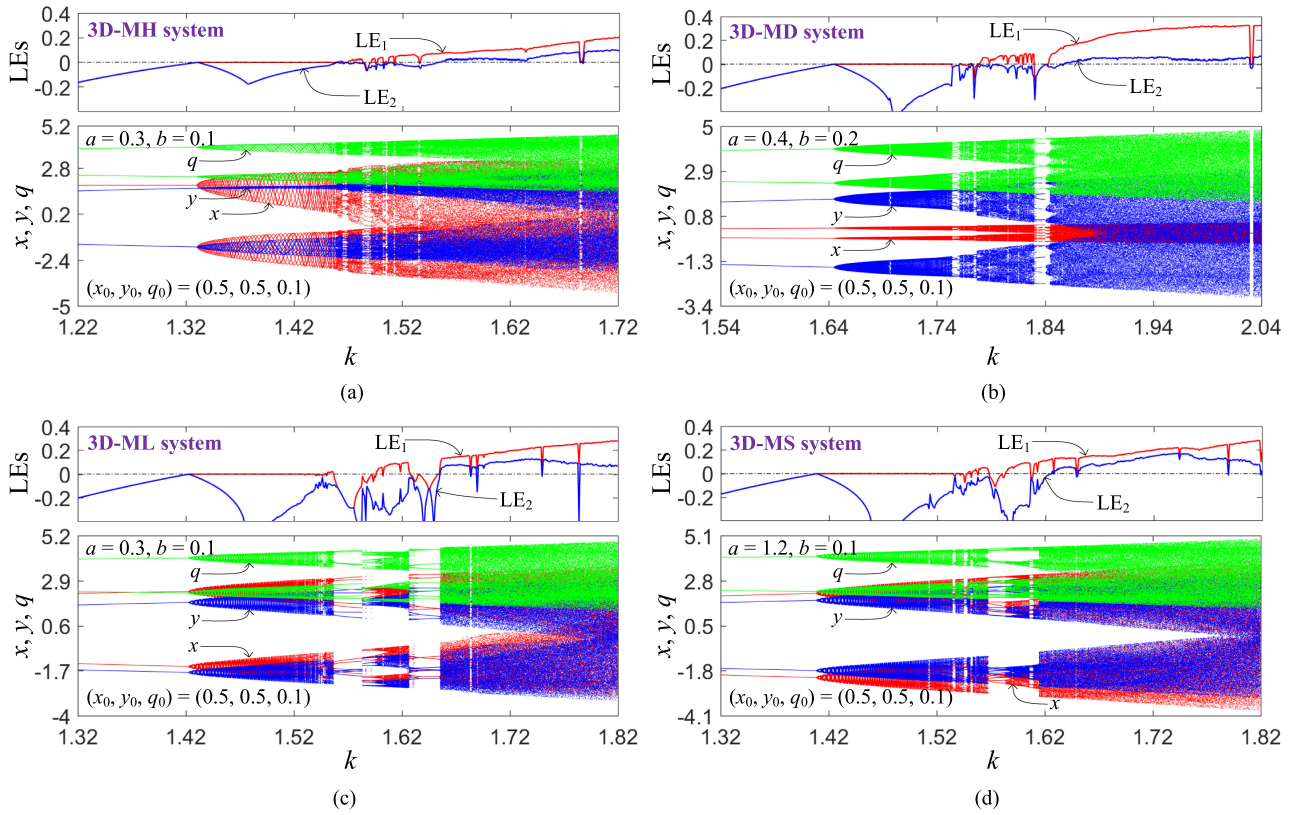


Fig. 2. For the four 3-D-DM maps, the coupling coefficient-depended bifurcation plots of three states x , y , and q (bottom) and first two LE spectra (top), where the typical parameters and initial states are marked. (a) Numerical plots of the 3-D-MH map with $k \in [1.22, 1.72]$. (b) Numerical plots of the 3-D-MD map with $k \in [1.54, 2.04]$. (c) Numerical plots of the 3-D-ML map with $k \in [1.32, 1.82]$. (d) Numerical plots of the 3-D-MS with $k \in [1.32, 1.82]$.

III. BIFURCATION DYNAMICS AND SEQUENCE PERFORMANCE

This section investigates the bifurcation dynamics of the four 3-D-DM maps using numerical measures and evaluates the performance of the hyperchaotic sequences generated by the four maps. For convenience, all the initials are assigned as $(x_0, y_0, q_0) = (0.5, 0.5, 0.1)$.

A. Bifurcation Dynamics and Hyperchaotic Attractors

When investigating the bifurcation behaviors of the four 3-D-DM maps, set the parameters a, b as two fixed values, and the coupling coefficient k as a bifurcation parameter. Fig. 2 shows the bifurcation plots of the three states x , y , and q , and the first two Lyapunov exponent (LE) spectra, where the LE spectra are calculated using the Wolf's Jacobian method. For the 3-D-DM maps, the typical settings of a, b , and variable intervals of k are marked in the respective diagrams in detail.

As shown in Fig. 2, when increasing k , all the four 3-D-DM maps undergo the quasi-periodic route to chaos and they can display hyperchaotic behaviors within relatively wide intervals. With the increment of k , the trajectories of these four maps first show periodic behaviors with negative first LE, and then enter into the quasi-periodic behaviors with zero first LE, and finally step into the chaotic behaviors with positive first LE via the quasi-periodic bifurcation scenarios. When the second LE becomes positive, these four maps exhibit the hyperchaotic behaviors. Besides, several periodic windows can be found in the chaos and hyperchaos intervals.

TABLE II
TYPICAL PARAMETERS AND LEs OF THE FOUR 3-D-DM MAPS

Map Types	Typical Parameters	LEs (LE ₁ , LE ₂ , LE ₃)
3D-MH Map	$a = 0.3, b = 0.1, k = 1.7$	0.1862, 0.0903, -0.2335
3D-MD Map	$a = 0.4, b = 0.2, k = 2$	0.3174, 0.0279, -1.5451
3D-ML Map	$a = 0.3, b = 0.1, k = 1.8$	0.2633, 0.0687, -1.2864
3D-MS Map	$a = 1.2, b = 0.1, k = 1.8$	0.2548, 0.1156, -2.4907

Table II shows the LEs of the four 3-D-DM maps under some typical parameter settings. With these parameter settings, all the four 3-D-DM maps have two positive LEs, indicating that they have hyperchaotic behaviors. As a contrast, the three existing 2-D discrete maps, namely the Hénon map, Duffing map, and Lozi map, have only one positive LE under typical parameter settings, implying that they cannot show hyperchaos.

Under these typical parameter settings listed in Table II, the phase plots projected on the x - y plane of the hyperchaotic attractors in the four 3-D-DM maps are displayed in Fig. 3. Fig. 3(a) and (b) shows that the hyperchaotic attractors involve only one complete piece, whereas Fig. 3(c) and (d) shows that the hyperchaotic attractors contain two separated pieces.

B. Hyperchaotic Sequences and Performance Indicators

Corresponding to the phase plots in Fig. 3, the hyperchaotic sequences under these typical parameter settings can be generated by the four 3-D-DM maps and they are shown in Fig. 4.

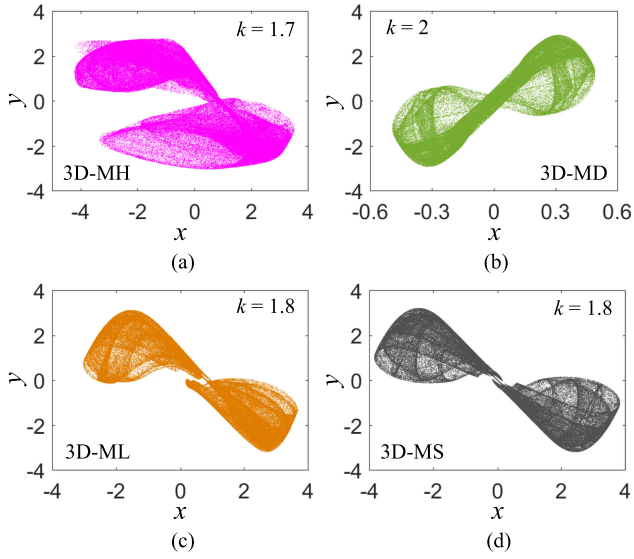


Fig. 3. Phase plots projected on the $x - y$ plane of the hyperchaotic attractors in the four 3-D-DM maps, where the typical coupling coefficients are marked. (a) 3-D-MH map with $k = 1.7$. (b) 3-D-MD map with $k = 2$. (c) 3-D-ML map with $k = 1.8$. (d) 3-D-MS map with $k = 1.8$.

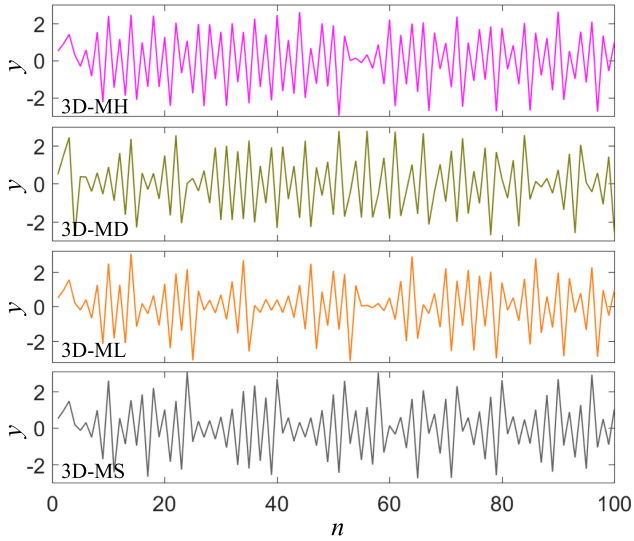


Fig. 4. Hyperchaotic sequences emerged from the four 3-D-DM maps under the typical parameter settings listed in Table II.

Because a hyperchaotic sequence usually shows better aperiodic and disordered properties than a chaotic sequence and it is thus more suitable for developing many chaos-based engineering applications. Note that the hyperchaotic sequences generated by the 3-D-MH and 3-D-ML maps are in hidden states, while those generated by the 3-D-MD and 3-D-MS maps are in self-excited states.

Similar to the performance analyses for the 2-D sine map presented by [28], the correlation dimension (CorDim), spectral entropy (SE), permutation entropy (PE), and Kaplan-Yorke dimension (D_{KY}) can be employed to evaluate the performance of the 3-D-DM hyperchaotic sequences. The length of these sequences is set as 50 000 and the calculated results are listed in Table III, from which the excellent performance indicators are demonstrated. This indicates that the memristor can greatly enhance the chaos complexity of existing 2-D discrete maps.

TABLE III
PERFORMANCE INDICTORS FOR THE 3-D-DM HYPERCHAOTIC SEQUENCES

Map Types	CorDim	SE	PE	D_{KY}
3D-MH Map	1.9397	0.6963	4.2847	3.0
3D-MD Map	1.7963	0.8763	4.0571	2.2283
3D-ML Map	1.8110	0.6149	3.7383	2.2644
3D-MS Map	1.7803	0.7196	3.7017	2.1479

IV. MEMRISTOR INITIAL-BOOSTED DYNAMICAL BEHAVIORS

Due to the DM, the bifurcation behaviors in the four 3-D-DM maps can be boosted by the memristor initials. This section studies the boosting mechanism theoretically and discloses the initial-boosted bifurcation behaviors numerically.

A. Memristor Initial-Boosted Dynamical Mechanism

To demonstrate the boosting mechanism by the memristor initial, the general 3-D-DM map model in (3) can be rewritten in an iterated equation form as

$$\begin{cases} x_{n+1} = F(x_n, y_n), \\ y_{n+1} = G(x_n) + k \cos \left(q_0 + \sum_{l=1}^{n-1} y_l \right) y_n. \end{cases} \quad (11)$$

For an integer number m , define a linear transformation as

$$q_0 = q_{00} + 2m\pi \quad (12)$$

in which q_{00} is used to compensate the memristor initial and it satisfies the following condition

$$-\pi < q_{00} + \sum_{l=1}^{n-1} y_l < \pi. \quad (13)$$

There yields

$$\cos \left(q_0 + \sum_{l=1}^{n-1} y_l \right) = \cos \left(q_{00} + \sum_{l=1}^{n-1} y_l \right) \quad (14)$$

which indicates the cyclic property of the memristance in (1).

Consequently, the general 3-D-DM map model is cyclic related to the memristor initial q_0 . The cyclic property can be verified by the invariance of the model (11) by utilizing the linear transformation in (12). It means that the dynamics of the 3-D-DM maps are cyclically altered by q_0 with period 2π . Therefore, all the 3-D-DM maps are boostable and their bifurcation behaviors can be boosted by the memristor initials.

B. Memristor Initial-Boosted Bifurcation Behaviors

The memristor initial-boosted bifurcation behaviors with the given parameter settings can be exhibited by one example of 3-D-DM maps, namely the 3-D-MS map.

Set the parameters and initials as $a = 1.2$, $b = 0.1$, $(x_0, y_0) = (0.5, 0.5)$, $q_0 = 0.1 + 2m\pi$ ($m = -2, -1, 0, 1$), and $k \in [1.32, 1.82]$. The coupling coefficient-depended bifurcation plots of the state q in the 3-D-MS map are simulated and their results are shown in Fig. 5. It can be found that the bifurcation plots under four fixed memristor initials can achieve the visually identical bifurcation structures. This result indicates that the coupling coefficient-depended bifurcation behaviors can be boosted in the dynamic ranges by q_0 with period 2π , which demonstrates

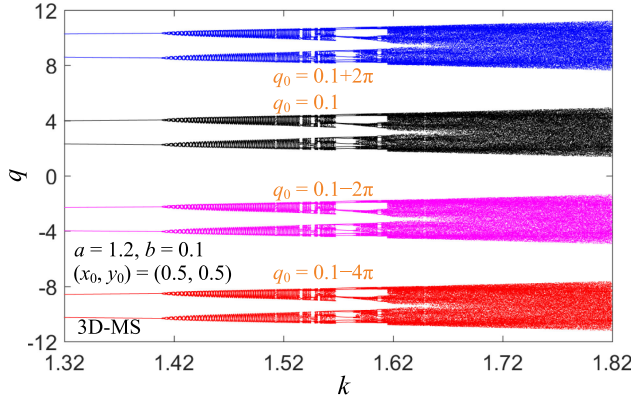


Fig. 5. For $a = 1.2$, $b = 0.1$, $(x_0, y_0) = (0.5, 0.5)$, and $q_0 = 0.1 + 2m\pi$ ($m = -2, -1, 0, 1$) with $k \in [1.32, 1.82]$, the memristor initial-boosted bifurcation behaviors along the q -axis.

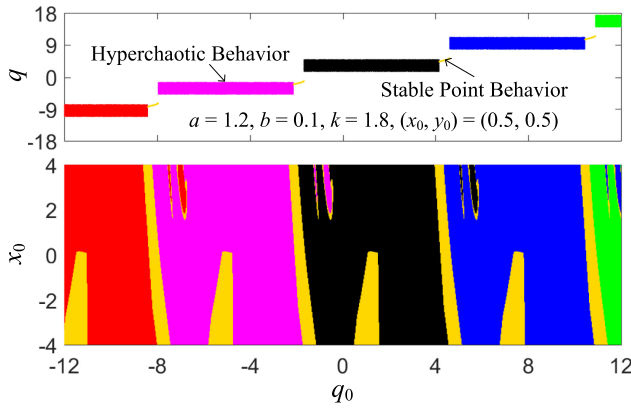


Fig. 6. For $a = 1.2$, $b = 0.1$, $k = 1.8$, and $y_0 = 0.5$, the local basin of attraction within $q_0 \in [-12, 12]$ and $x_0 \in [-4, 4]$ (bottom) and bifurcation plot of the memristor state q with determined $(x_0, y_0) = (0.5, 0.5)$ (top).

the feasibility of theoretical analysis mentioned above. Besides, when increasing m to infinity, infinitely many initial-boosted bifurcations are achieved on the dimension q , which indicates the coexistence of infinite attractors in the 3-D-MS map.

As listed in Table II, the typical parameters of the 3-D-MS map are set as $a = 1.2$, $b = 0.1$, and $k = 1.8$. To measure the long-term behaviors of each initial in the 3-D-MS map, the local basin of attraction in the $x_0 - q_0$ initial plane is shown in Fig. 6 (bottom). There are numerous boundaries that divide the attracting regions of hyperchaotic attractors with different dynamic ranges and stable points with different positions. Correspondingly, an example of memristor initial-boosted bifurcation plot for determined $x_0 = 0.5$ is also plotted in Fig. 6 (top). The blocks marked as red, magenta, black, blue, and green correspond to the colorful regions of hyperchaotic attractors with different dynamic ranges. The orange lines correspond to the orange regions of stable points with different positions. The results in Fig. 6 demonstrate that the dynamical behaviors in the 3-D-MS map are completely depended on the memristor initial. The similar results can also be found in the other D-DM maps.

C. Memristor Initial-Switched Attractors and Sequences

For the typical parameter settings $a = 1.2$, $b = 0.1$, $k = 1.8$, and $(x_0, y_0) = (0.5, 0.5)$, when assigning the memristor initial as

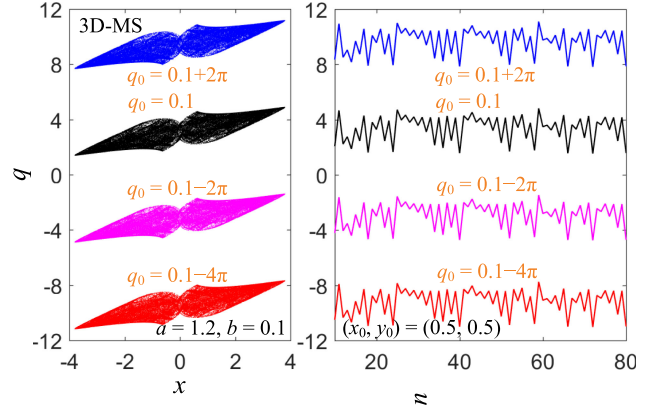


Fig. 7. For $a = 1.2$, $b = 0.1$, $k = 1.8$, $(x_0, y_0) = (0.5, 0.5)$, and $q_0 = 0.1 + 2m\pi$ ($m = -2, -1, 0, 1$), memristor initial-switched hyperchaotic attractors (left) and sequences (right) of the 3-D-MS map, manifesting the hyperchaos robustly switched by the memristor initial.

TABLE IV
PERFORMANCE INDICATORS FOR MEMRISTOR INITIAL-SWITCHED HYPERCHAOS

Initial q_0	LE ₁ , LE ₂	CorDim	SE	PE
$0.1 + 2\pi$	0.2551, 0.1112	1.7567	0.7222	3.6975
0.1	0.2568, 0.1111	1.7803	0.7196	3.7017
$0.1 - 2\pi$	0.2581, 0.1161	1.7690	0.7205	3.7159
$0.1 - 4\pi$	0.2593, 0.1111	1.7475	0.7206	3.7117

$q_0 = 0.1 + 2m\pi$ ($m = -2, -1, 0, 1$), four sets of hyperchaotic attractors and sequences can be generated by the 3-D-MS map and they are depicted in Fig. 7. The numerical results further indicate that the dynamic ranges of the hyperchaotic attractors and sequences can be robustly switched by the memristor initial with period 2π along the q -axis.

The same indicators shown in Tables II and III are adopted to evaluate the performance of the memristor initial-switched hyperchaos. Table IV lists the test results of the hyperchaotic sequences plotted in Fig. 7. As can be seen, the memristor initial-switched hyperchaos can obtain almost the same results. The slight differences are caused by the calculation errors. This indicates that the hyperchaotic sequences generated by the 3-D-MS map can be controlled by the memristor initial and the memristor initial-switched hyperchaos is robust.

V. HARDWARE EXPERIMENT AND APPLICATION IN AC-GANs

This section implements the four 3-D-DM maps in a hardware platform and applies them to generate PRNs. Taking the PRNs as latent variables, a chaos-based application in AC-GANs is further explored.

A. Microcontroller-Based Hardware Experiment

The STM32F407 family is a high-performance device that contains the ARM Cortex-M4 32-bit RISC core. Using such a powerful microcontroller, a functional hardware platform is readily developed to implement the 3-D-DM maps. The platform includes the microcontroller STM32F407VET6, D/A converter TLV5618, and simple level translation circuit. The level translation circuit is constructed by an op-amp AD711AH and three

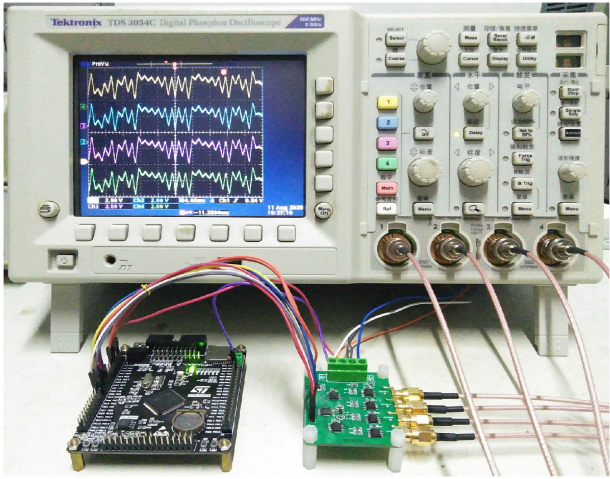


Fig. 8. Experimental prototype of the hardware platform connected with a four-channel digital oscilloscope.

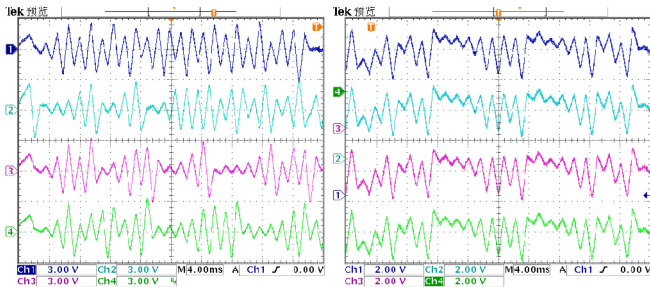


Fig. 9. Measured four-channel voltage sequences from the hardware platform. (a) Hyperchaotic sequences generated by the four 3-D-DM maps. (b) Memristor initial-switched hyperchaotic sequences of the 3-D-MS map.

resistors. In the platform, the microcontroller implements a full set of operation instructions of the 3-D-DM maps, the D/A converter outputs the unipolar analog voltage sequences, and the level translation circuit transmits the bipolar analog voltage sequences to a digital oscilloscope.

The 3-D-DM maps presented in Table I are programmed using C language and their software codes are then downloaded to the microcontroller. The typical parameters and initials are set as the values in Tables II and III, respectively, and they are preloaded to the hardware platform. After executing the program software, the four-channel voltage sequences can be synchronously generated by the 3-D-DM maps.

The snapshot of experimental prototype is provided in Fig. 8. First, the hyperchaotic voltage sequences of the 3-D-MH, 3-D-ML, 3-D-MD, and 3-D-MS maps are concurrently outputted from the hardware platform and the results are synchronously displayed in Fig. 9(a). Then for the 3-D-MS map, the four-channel hyperchaotic voltage sequences are generated with four different memristor initials and displayed in Fig. 9(b). As can be seen, the experimental results are consistent with the numerical results in Figs. 4 and 7. This verifies the feasibility of hardware implementation of the 3-D-DM maps. Notably, the hardware platform is digital rather than analog. Of course, the 3-D-DM maps can be also implemented in analog. However, when implemented in analog, the memristor initials cannot be preset so that

TABLE V
NIST TEST RESULTS OF THE PRNs GENERATED BY TWO 3-D-DM MAPS

No.	Sub-tests	3D-MH Map		3D-MS Map	
		Pass rate	P-value _T	Pass rate	P-value _T
		≥ 0.9856	≥ 0.0001	≥ 0.9856	≥ 0.0001
01	Frequency	0.9904	0.9972	0.9909	0.6720
02	Block Frequency	0.9910	0.9930	0.9906	0.6421
03	Cum. Sums* (F)	0.9903	0.8315	0.9892	0.8742
	Cum. Sums* (R)	0.9917	0.8308	0.9900	0.7849
04	Runs	0.9975	0.7152	0.9887	0.8484
05	Longest Runs	0.9888	0.7444	0.9895	0.7321
06	Rank	0.9914	0.0343	0.9909	0.1604
07	FFT	0.9882	0.0002	0.9885	0.0049
08	Non-Ovla. Temp.*	0.9898	0.4678	0.9898	0.5017
09	Ovla. Temp.	0.9889	0.2179	0.9893	0.0632
10	Universal	0.9896	0.0885	0.9884	0.8995
11	Appr. Entropy	0.9903	0.5059	0.9905	0.0837
12	Ran. Exc.*	0.9912	0.5893	0.9882	0.3078
13	Ran. Exc. Var.*	0.9907	0.6604	0.9901	0.3708
14	Serial (1st)	0.9887	0.5516	0.9888	0.2802
	Serial (2nd)	0.9880	0.8518	0.9887	0.5304
15	Linear complexity	0.9890	0.2649	0.9889	0.5329
	Success No.	15/15	15/15	15/15	15/15

*Non-Ovla. Temp., Ran. Exc., and Ran. Exc. Var. tests are comprised of 148, 8, and 18 subtests, respectively. The average result of multiple sub-tests is reported.

the generated hyperchaotic sequences cannot be directly used in practical applications.

B. PRN Generation and NIST Test

Because of the unique properties of the initial sensitivity and unpredictability, the chaotic sequences generated by the chaotic maps are often used as PRNs [8], [28]. Since the presented 3-D-DM maps have complex dynamics, their generated PRNs have high randomness [29], [30]. In this subsection, the 3-D-MH and 3-D-MS maps are taken as two examples of the 3-D-DM map to generate PRNs.

Denote $Y = \{Y(1), Y(2), \dots, Y(n), \dots\}$ as a chaotic sequence generated by a chaotic map. First, change each of $Y(n)$ to be a 52-bit binary stream $Y_B(n)$ by employing the IEEE 754 float standard, and then 8 bits of PRNs can be obtained by taking the binaries from the 35-th bit to 42-th bit in $Y_B(n)$, which can be described as

$$P_i = Y_B(n)_{35:42}. \quad (15)$$

Clearly, each output state can generate 8 bits of PRNs.

In our experiments, 8000 binary sequences with 10^6 bits in each sequence (a total number of 8 G bits) are separately generated by the 3-D-MH and 3-D-MS maps, and tested by the NIST SP800-22 test suite [31]. The test suite has 15 subtests and the PRNs can pass the subtest if the obtained pass rate is larger than 0.9856 and the P -value_T is larger than 0.0001, according to the discussions in [31]. Table V lists the test results of the PRNs generated by the 3-D-MH and 3-D-MS maps. As can be seen, the generated 8 Gb PRNs can pass all the sub-tests, further indicating the high complexity and high availability of the presented 3-D-DM maps.

C. Chaos-Based Application in AC-GANs

The famous GANs are the network architectures for training deep generative models [18]. The generative net can generate

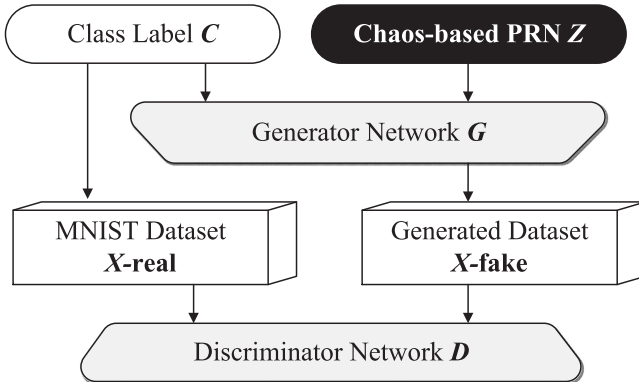


Fig. 10. Training framework of the AC-GANs using the chaos-based PRNs as the latent variables.

highly realistic data by using an adversarial mechanism between the generator and the discriminator. In the training process, the GANs require a large number of PRNs and the current strategy usually uses the Gaussian white noise generated by a computer as the PRNs.

Since the PRNs generated by the 3-D-DM maps have high randomness and the chaos-based PRNs are easily generated by our developed hardware platform, they are suitable for the application of GANs [24]. In this subsection, we employ the three existing 2-D discrete maps and four 3-D-DM maps to generate the chaos-based PRNs for replacing the noise-based PRNs in the GANs.

To improve the training-stability and discriminability in the image generation, AC-GANs were proposed as an extension of the GANs [23]. The latent variables of the AC-GANs are the chaos-based PRNs by the existing 2-D discrete maps and presented 3-D-DM maps acquired from our hardware platform. Then a training framework of the chaos-based AC-GANs can be constructed and is shown in Fig. 10. The chaos-based AC-GANs have two networks: the generator network G and discriminator network D . The input vector $Z = \{x_1, y_1, x_2, y_2, \dots, x_n, y_n\}$ for G consists of the chaos-based PRNs, which are constructed by successively combining the first two chaotic/hyperchaotic sequences of a 2-D/3-D discrete map mentioned above, instead of digitally encoding and reconstructing the chaotic sequences in [24]. The mini-batch size in the stochastic gradient descent method is also set as 100 and the learning rate in Adam optimizer is set as 0.0002 for training. Besides, the MNIST database in [32] is used and it contains 60 000 training sets and 10 000 test sets.

The chaos-based PRN Z and class label C are the two inputs of the generator network G . A fully-connected layer is first created for sampling the input and a new convolution layer with the depth 384 and feature map 3×3 is thereby constructed. There are total three transposed convolution layers, in which the size of all the kernels is 5×5 and the sizes of the respective strides are $[1, 2, 2]$. After three times of up-sampling, a figure with size 28×28 can be finally generated. Note that the ReLU activation function is used for each transposed convolution after batch normalization, and the tanh activation function is used for the output layer.

When inputting an image of size 28×28 , the discriminator network D can output the probability of real image and the probability of belonging to each known class. The D is constructed by four convolution layers and two fully connected

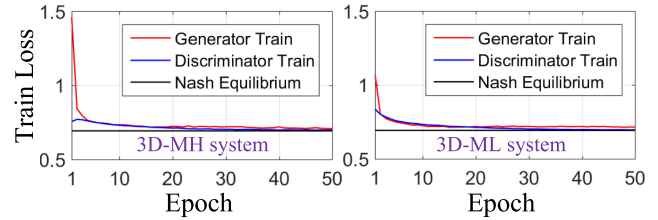


Fig. 11. Train losses of the chaos-based AC-GANs.

TABLE VI
CLASSIFICATION ACCURACIES USING DIFFERENT CHAOS-BASED PRNs

PRNs	Hénon Map	Duffing Map	Lozi Map	Simple Map
Class. Accuracy	0.99590	0.99640	0.99592	-
PRNs	MH Map	MD Map	ML Map	MS Map
Class. Accuracy	0.99625	0.99645	0.99615	0.99580

layers, where the convolution layers act as the implicit layers while the connected layers act as the output layers. For the four convolution layers, the size of all their kernels is 3×3 , the sizes of their respective strides are set as $[2, 1, 2, 1]$, and the depths of their respective networks are set as $[32, 64, 128, 256]$. After each convolution operation, the data goes through leaky ReLU and Dropout. In the two output layers, the sigmoid function is used for judging the real or fake image and the softmax function is used for predicting the probabilities of each class label.

The availability of the chaos-based PRNs applied to the AC-GANs can be verified by the train losses of G and D , which is shown in Fig. 11. As can be seen, the train losses of the AC-GANs quickly converge to the Nash equilibrium at around the 10th epoch. This indicates that the chaos-based PRNs generated by the 3-D-DM maps can be used in the training process of AC-GANs.

To compare the training effects, the noise-based PRNs and chaos-based PRNs are separately used as the latent variables. Note that the noise is generated using the built-in function in the Python programming language with average 0 and standard deviation 1. The discriminator accuracies for D during training are depicted in Fig. 12. As can be demonstrated, when increasing the training epoch, the generator using the PRNs generated by the existing 2-D discrete maps can produce similar discriminator accuracy than it using the PRNs generated by noise, while the generator using the PRNs generated by the presented 3-D-DM maps can yield higher discriminator accuracy and faster upward-trending. This is because the 3-D-DM maps can generate PRNs with high randomness that can enhance the fitting rate of the generation function. After 50 epochs training, the final classification accuracies can be obtained and are shown in Table VI. Note that the final classification accuracy using the noise-based PRNs is 0.99615. As can be observed from Table VI, the discriminator D can also achieve high classification accuracies when using the PRNs generated by different chaotic systems. Besides, except for the simple discrete map, all the other 2-D/3-D discrete maps can generate PRNs with high randomness. Therefore, when using the PRNs generated by the 3-D-DM maps as the latent variables in the AC-GANs, the final classification accuracy is improved only a little, but the discriminator accuracy is greatly improved.

Moreover, to show a visual effect about the generation results of the AC-GANs when separately using the PRNs by noise and

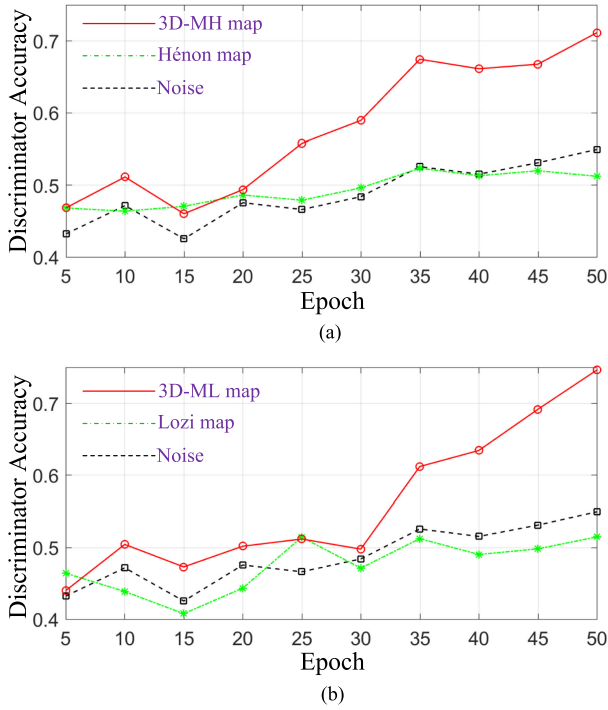


Fig. 12. When increasing the training epochs, the discriminator accuracies on MNIST database using the noise-based PRNs and chaos-based PRNs. (a) Chaos-based PRNs generated by 3-D-MH map and Hénon map. (b) Chaos-based PRNs generated by 3-D-ML map and Lozi map.

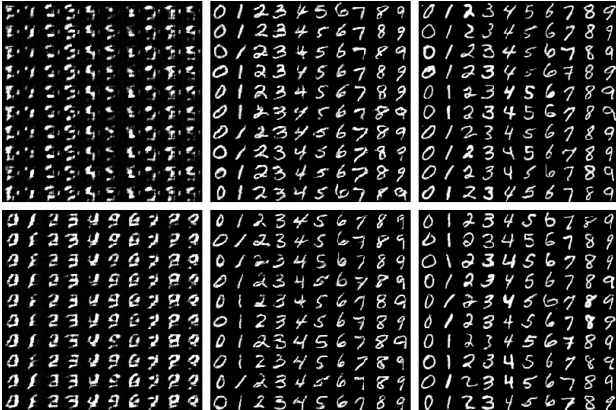


Fig. 13. Handwritten images generated with training at the 1st epoch, 10th epoch, and 50th epoch using the noise-based PRNs (the top row) and chaos-based PRNs (the bottom row).

the PRNs by the 3-D-MS map as the latent variables, Fig. 13 plots the representative examples of handwritten images trained at the 1st epoch, 10th epoch, and 50th epoch, respectively. As can be seen, the AC-GANs using the PRNs by the 3-D-MS map can exhibit excellent training effects.

VI. CONCLUSION

In this article, we presented a general 3-D-DM map model and provided four examples of hyperchaotic maps. In these four 3-D-DM maps, two maps with no fixed points were in hidden states, while the other two maps with infinitely many fixed

points were in self-excited states. The results showed that the memristor can enhance the chaos complexity and its coupling map can display hyperchaos with excellent performance indicators. Notably, the hyperchaotic attractors and sequences can be switched by the memristor initials. This property allowed the 3-D-DM maps to have many advantages in engineering applications. In addition, the hardware platform was developed to implement these maps and the acquired voltage sequences have high randomness. The hyperchaotic sequences were applied to the AC-GANs as the latent variables. Performance analyses showed that the hyperchaotic sequences can greatly improve the discriminator accuracy of the AC-GANs. Certainly, developing new DM models and their coupling dynamical systems as well as implementing the 3-D-DM map-based PRNG for AC-GANs on ImageNet database [33], GANs-based password guessing [34], [35], and BigGANs [36], deserved our further study.

REFERENCES

- T. Prodromakis, C. Toumazou, and L. Chua, "Two centuries of memristors," *Nature Mater.*, vol. 11, no. 6, pp. 478–481, Jun. 2012.
- L. Chua, "If it's pinched it's a memristor," *Semicond. Sci. Technol.*, vol. 29, no. 10, Sep. 2014, Art. no. 104001.
- M. Chen, M. Sun, H. Bao, Y. Hu, and B. Bao, "Flux-charge analysis of two-memristor-based chua's circuit: Dimensionality decreasing model for detecting extreme multistability," *IEEE Trans. Ind. Electron.*, vol. 67, no. 3, pp. 2197–2206, Mar. 2020.
- P. Yao et al., "Fully hardware-implemented memristor convolutional neural network," *Nature*, vol. 577, no. 7550, pp. 641–646, Jan. 2020.
- Z. Hua, B. Zhou, and Y. Zhou, "Sine chaotification model for enhancing chaos and its hardware implementation," *IEEE Trans. Ind. Electron.*, vol. 66, no. 2, pp. 1273–1284, Feb 2019.
- C. Li, D. Lin, J. Liu, and F. Hao, "Cryptanalyzing an image encryption algorithm based on autblocking and electrocardiography," *IEEE MultiMedia*, vol. 25, no. 4, pp. 46–56, Oct.–Dec. 2018.
- X. Meng, P. Rozycki, J.-F. Qiao, and B. M. Wilamowski, "Nonlinear system modeling using RBF networks for industrial application," *IEEE Trans. Ind. Informat.*, vol. 14, no. 3, pp. 931–940, Mar. 2018.
- L. Yin, Z. Deng, B. Huo, and Y. Xia, "Finite-time synchronization for chaotic gyros systems with terminal sliding mode control," *IEEE Trans. Syst., Man, Cybern., Syst.*, vol. 49, no. 6, pp. 1131–1140, Jun. 2019.
- D. Abbasinezhad-Mood and M. Nikooghadam, "Efficient anonymous password-authenticated key exchange protocol to read isolated smart meters by utilization of extended Chebyshev chaotic maps," *IEEE Trans. Ind. Informat.*, vol. 14, no. 11, pp. 4815–4828, Nov. 2018.
- H. Bao, A. Hu, W. Liu, and B. Bao, "Hidden bursting firings and bifurcation mechanisms in memristive neuron model with threshold electromagnetic induction," *IEEE Trans. Neural Netw. Learn. Syst.*, vol. 31, no. 2, pp. 502–511, Feb. 2020.
- P. Jin, G. Wang, H. H.-C. Iu, and T. Fernando, "A locally active memristor and its application in a chaotic circuit," *IEEE Trans. Circuits Syst. II, Exp. Briefs*, vol. 65, no. 2, pp. 246–250, Feb. 2018.
- Q. Lai, P. D. K. Kuat, F. Liu, and H. H. Iu, "An extremely simple chaotic system with infinitely many coexisting attractors," *IEEE Trans. Circuits Syst. II, Exp. Briefs*, vol. 67, no. 6, pp. 1129–1133, Jun. 2020.
- H. Bao, M. Chen, H. Wu, and B. Bao, "Memristor initial-boosted coexisting plane bifurcations and its extreme multi-stability reconstitution in two-memristor-based dynamical system," *Sci. China Technol. Sci.*, vol. 63, no. 4, pp. 603–613, Apr. 2020.
- B. Bao, H. Li, H. Wu, X. Zhang, and M. Chen, "Hyperchaos in a second-order discrete memristor-based map model," *Electron. Lett.*, vol. 56, no. 15, pp. 769–770, Jul. 2020.
- H. Li, Z. Hua, H. Bao, M. Chen, and B. Bao, "Two-dimensional memristive hyperchaotic maps and application in secure communication," *IEEE Trans. Ind. Electron.*, vol. 68, no. 10, pp. 9931–9940, Oct. 2021.
- Y. Peng, K. Sun, and S. He, "A discrete memristor model and its application in hénón map," *Chaos Solitons Fract.*, vol. 137, Aug. 2020, Art. no. 109873.
- Y. Deng and Y. Li, "Nonparametric bifurcation mechanism in 2-D hyperchaotic discrete memristor-based map," *Nonlinear Dyn.*, vol. 104, pp. 4601–4614, Jun. 2021.

- [18] I. Goodfellow *et al.*, “Generative adversarial nets,” in *Proc. Adv. Neural Inf. Process. Syst.*, 2014, pp. 2672–2680.
- [19] F. L. Han, H. B. Zhang, S. Chatterjee, Q. Guo, and S. L. Wan, “A modified generative adversarial nets integrated with stochastic approach for realizing super-resolution reservoir simulation,” *IEEE Trans. Geosci. Remote Sens.*, vol. 58, no. 2, pp. 1325–1336, Feb. 2020.
- [20] J. Liu, F. Qu, X. Hong, and H. Zhang, “A small-sample wind turbine fault detection method with synthetic fault data using generative adversarial nets,” *IEEE Trans. Ind. Informat.*, vol. 15, no. 7, pp. 3877–3888, Jul. 2019.
- [21] P. Liang, C. Deng, J. Wu, G. Li, Z. Yang, and Y. Wang, “Intelligent fault diagnosis via semi-supervised generative adversarial nets and wavelet transform,” *IEEE Trans. Instrum. Meas.*, vol. 69, no. 7, pp. 4659–4671, Jul. 2020.
- [22] X. Xia, R. Tongeri, F. Sohel, and D. Huang, “Auxiliary classifier generative adversarial network with soft labels in imbalanced acoustic event detection,” *IEEE Trans. Multimedia*, vol. 21, no. 6, pp. 1359–1371, Jun. 2019.
- [23] A. Odena, C. Olah, and J. Shlens, “Conditional image synthesis with auxiliary classifier GANs,” in *Proc. 34th Int. Conf. Mach. Learn.*, 2017, pp. 2642–2651.
- [24] M. Naruse, T. Matsubara, N. Chauvet, K. Kanno, T. Yang, and A. Uchida, “Generative adversarial network based on chaotic time series,” *Sci. Rep.*, vol. 9, Sep. 2019, Art. no. 12963.
- [25] M. Hénon, “A two-dimensional mapping with a strange attractor,” *Commun. Math. Phys.*, vol. 50, no. 1, pp. 69–77, Feb. 1976.
- [26] R. L. Devaney, *Fractal Patterns Arising in Chaotic Dynamical Systems*. Vienna, Austria: Springer, 1988, pp. 137–168.
- [27] V. Botella-Soler, J. M. Castelo, J. A. Oteo, and J. Ros, “Bifurcations in the lozi map,” *J. Phys. A: Math. Theor.*, vol. 44, no. 30, Jun. 2011, Art. no. 305101.
- [28] H. Bao, Z. Hua, N. Wang, L. Zhu, M. Chen, and B. Bao, “Initials-boosted coexisting chaos in a 2-D sine map and its hardware implementation,” *IEEE Trans. Ind. Informat.*, vol. 17, no. 2, pp. 1132–1140, Feb. 2021.
- [29] M. Bakiri, C. Guyeux, J.-F. Couchot, L. Marangio, and S. Galatolo, “A hardware and secure pseudorandom generator for constrained devices,” *IEEE Trans. Ind. Informat.*, vol. 14, no. 8, pp. 3754–3765, Aug. 2018.
- [30] Z. Hua, Y. Zhou, and B. Bao, “Two-dimensional sine chaotification system with hardware implementation,” *IEEE Trans. Ind. Informat.*, vol. 16, no. 2, pp. 887–897, Feb. 2020.
- [31] A. L. B. III *et al.*, “SP 800-22 Rev. 1a. A statistical test suite for random and pseudorandom number generators for cryptographic applications,” Nat. Inst. Std. Technol., Gaithersburg, MD, USA, Tech. Rep. SP 800-22, 2010.
- [32] E. Kussul and T. Baidyk, “Improved method of handwritten digit recognition tested on MNIST database,” *Image Vis. Comput.*, vol. 22, no. 12, pp. 971–981, Oct. 2004.
- [33] J. Deng, W. Dong, R. Socher, L. Li, K. Li, and F. Li, “ImageNet: A large-scale hierarchical image database,” in *Proc. IEEE Conf. Comput. Vis. Pattern Recognit.*, 2009, pp. 248–255.
- [34] D. Wang, Z. Zhang, P. Wang, J. Yan, and X. Huang, “Targeted online password guessing: An underestimated threat,” in *Proc. ACM SIGSAC Conf. Comput. Commun. Secur.*, 2016, pp. 1242–1254.
- [35] D. Wang, H. Cheng, P. Wang, X. Huang, and G. Jian, “Zipf’s law in passwords,” *IEEE Trans. Inf. Forensics Secur.*, vol. 12, no. 11, pp. 2776–2791, Nov. 2017.
- [36] A. Brock, J. Donahue, and K. Simonyan, “Large scale GAN training for high fidelity natural image synthesis,” in *Proc. Int. Conf. Learn. Representations*, 2019, pp. 1–35.



Han Bao (Member, IEEE) received the B.S. degree in landscape design from the Jiangxi University of Finance and Economics, Nanchang, China, in 2015, and the M.S. degree in art and design from Changzhou University, Changzhou, China, in 2018. He is currently working toward the Ph.D. degree in nonlinear system analysis and measurement technology with the Nanjing University of Aeronautics and Astronautics, Nanjing, China, and is undergoing a one-year joint training with Changzhou University, Changzhou, China.

In 2019, he visited the Computer Science Department, The University of Auckland, New Zealand. His research interests include memristive neuromorphic circuit, nonlinear circuits and systems, and artificial intelligence.



Zhongyun Hua (Member, IEEE) received the B.S. degree from Chongqing University, Chongqing, China, in 2011, and the M.S. and Ph.D. degrees from the University of Macau, Macau, China, in 2013 and 2016, respectively, all in software engineering.

He is currently an Associate Professor with the School of Computer Science and Technology, Harbin Institute of Technology, Shenzhen, Shenzhen, China. His research interests include chaotic system, chaos-based applications, multimedia security, and data hiding.



systems.

Houzhen Li (Graduate Student Member, IEEE) received the B.S. degree in optoelectronic information science and engineering from the Changshu Institute of Technology, Suzhou, China, in 2019. He is currently working toward the M.S. degree in electronics science and technology with the School of Microelectronics and Control Engineering, Changzhou University, Changzhou, China.

His research interests include memristive neuromorphic circuit and nonlinear circuits and



Mo Chen (Member, IEEE) received the B.S. degree in information engineering, the M.S. degree in electromagnetic field and microwave technology, and the Ph.D. degree in electromagnetic field and microwave technology from Southeast University, Jiangsu, China, in 2003, 2006, and 2009, respectively.

Between 2009 and 2013, she was a Lecturer with Southeast University, Nanjing, China. She is currently an Associate Professor with the School of Microelectronics and Control Engineering, Changzhou University, Changzhou, China. Her research interest includes memristor and its application circuits and other nonlinear circuits and systems.



Bocheng Bao (Member, IEEE) received the B.S. and M.S. degrees in electronic engineering from the University of Electronics Science and Technology of China, Chengdu, China, in 1986 and 1989, respectively, and the Ph.D. degree in information and communication engineering, from the Nanjing University of Science and Technology, Nanjing, China, in 2010.

From 2008 to 2011, he was a Professor with the School of Electrical and Information Engineering, Jiangsu University of Technology, Changzhou, China. He was a Professor with the School of Microelectronics and Control Engineering, Changzhou University, Changzhou. In 2013, he visited the Department of Electrical and Computer Engineering, University of Calgary, Calgary, AB, Canada. His research interests include neuromorphic circuits, power electronic circuits, and nonlinear circuits and systems.

Dr. Bao was the recipient of the IET Premium Award in 2018 and selected as the Highly Cited Researcher 2020 in Cross-Field.